

Title: Strong sensitivity of Pine Island ice shelf melting to climatic variability

Authors: Pierre Dutrieux^{1*}, Jan De Rydt¹, Adrian Jenkins¹, Paul R. Holland¹, Ho Kyung Ha², Sang Hoon Lee², Eric J. Steig³, Qinghua Ding³, E. Povl Abrahamsen¹, Michael Schröder⁴

5 Affiliations:

¹British Antarctic Survey, NERC, Cambridge, UK.

²Korea Polar Research Institute, KIOST, Incheon, Korea.

³Department of Earth and Space Sciences and Quaternary Research Center, University of Washington, Seattle, WA, USA.

10 ⁴Alfred-Wegener-Institute for Polar and Marine Research, Bremerhaven, Germany.

*Correspondence to: pierre.dutrieux@bas.ac.uk

Abstract: Pine Island Glacier has thinned and accelerated over recent decades, significantly contributing to global sea level rise. Increased oceanic melting of its ice shelf is thought to have triggered those changes. Observations and numerical modeling reveal large fluctuations in the ocean heat available in the adjacent bay and enhanced sensitivity of ice shelf melting to water temperatures at intermediate depth, as a seabed ridge blocks the deepest and warmest waters from reaching the thickest ice. Oceanic melting decreased by 50% between January 2010 and 2012, with ocean conditions in 2012 partly attributable to atmospheric forcing associated with a strong La Niña event. Both atmospheric variability and local ice shelf and seabed geometry play fundamental roles in determining the response of the Antarctic Ice Sheet to climate.

One Sentence Summary: Ocean melting of the Pine Island Glacier ice shelf was halved in two years as an underlying seabed ridge makes it highly sensitive to climatic forcing.

25 Main Text:

Austral summer observations in the Amundsen Sea, West Antarctica, show that lightly-modified, warm (0.5-1.2°C) and saline (>34.6) Circumpolar Deep Water (CDW), 2-4°C above the in-situ freezing point, pervades a network of glacially scoured seabed troughs (1, Fig. 1A). The CDW reaches nearby Antarctic glaciers and delivers heat to the base of their 200-1000 m-thick ice shelves (2-4). It is overlain by a 200-300 m-thick layer of cold (-1.5°C) and fresh (salinity<34.4) Winter Water (WW, Fig. 2A) that is seasonally replenished by interaction with the atmosphere and sea ice.

Pine Island Glacier (PIG), a major outlet glacier feeding one such ice shelf, has shown apparently continuous thinning (5, 6) and intermittent acceleration (7-9) from 1973 to 2009. During this period, its ice shelf has also thinned (6, 10-12), and the reduction in buttressing driven by oceanic melting is believed to be responsible for the changes inland. Earlier analysis indicated that a higher CDW volume and temperature in Pine Island Bay (PIB) in January 2009 caused an increase in ice-shelf melting and in the associated meltwater-driven circulation,

relative to 1994 (2). The lack of sub-annual variability in CDW temperature during one year-long measurement in PIB (1) and the long-term correlation between the oceanic melting and the mass loss required to sustain thinning of the ice shelf gave the impression that the ice-ocean system had shown progressive change over the last two decades. This is consistent with a positive geometrical feedback, with oceanic melt enlarging the cavity under the ice shelf, allowing stronger circulation and further melting.

However, such ice-ocean systems are likely to be more complex. The glacier's rapid change over the last few decades was probably triggered by its ungrounding from a the top of a seabed ridge transverse to the ice flow at some time before the 1970s (4). Subsequent migration of the glacier's grounding line (13) down the seabed slope upstream from the ridge crest was probably an inevitable response (14), which had a major impact on cavity geometry, but projections of future evolution remain unclear (15–17). In this context, climate-driven variability of the delivery of heat to the ice sheet margin may be important (18). To understand the relative roles of glacier dynamics and climate variability in driving past, present and future glacier evolution requires knowledge of the spatial (19, 20, Fig. 1C) and temporal variability of ocean-driven melting.

Ocean simulations with a varying degree of horizontal resolution and using poorly-constrained seabed and ice geometry produce a broad spectrum of variability in CDW volume in PIB (21) and oceanic melt of PIG (22). Some studies suggest that basal melt is sensitive to the strength of the circulation in the Amundsen Sea (22). Others associate its variability with changing wind-driven inflow of warm CDW at the continental shelf edge and temperature variability at the calving front of the glacier (21, 23) impacted by far-field forcing of the atmospheric circulation (18). All these ocean/atmosphere sensitivities are linked dynamically, but a clear consensus on the most important driver of melt variability is lacking.

Hydrographic observations made in January 2012 in the eastern Amundsen Sea complement previous surveys from 1994, 2000, 2007, 2009 (2) and 2010 (24, Fig. 1B), and offer a new perspective. Indeed, though near-bottom 2012 CDW temperatures of 1.2°C are very similar to the warmest records (2007, 2009 and 2010), the available heat reaching the PIG calving front is significantly reduced. The top of the thermocline (the depth at which temperature first increases sharply with increasing depth) is about 250 m deeper compared with any other year for which measurements exist (Figs. 2A, 3A and 3B). Furthermore, the 2012 thermocline is

sharpened such that the temperature increases from -0.8 to 0.8°C over only 180 m, compared
70 with 250-350 m for other summers (Fig. 2A).

The temperature change occurring between 2010 and 2012 is largely associated with a salinity change, implying either that anomalies in the regional surface buoyancy or wind forcing cooled the upper thermocline through diapycnal exchanges (25); or that remote modifications in the atmosphere-ocean system led to decreased isopycnal advection of CDW from the continental shelf edge (21); or both. Thermocline depth changes in PIB are generally expected to occur at
75 intraseasonal to interannual timescales (21, 22), but the few synoptic summer observations available do not allow us to assess the origin, magnitude, frequency or duration of such variability. Hydrographic profiles taken at the continental shelf edge in the troughs leading to PIB (Figs. 2C and 2D) show that the western trough has a deeper and more variable thermocline
80 than the eastern trough, consistent with the warmest inflows being found in the east (Fig. 1A), but heavy sea ice prevented sampling in the eastern trough in 2012.

Another observation is that a temperature decrease of $0.4\text{-}1^{\circ}\text{C}$ occurred in 2012 at the location of previously identified meltwater outflows (2, around 400 m depth, Fig. 2B), and this must be associated with changes in the ice shelf-ocean interaction. Derived ice-shelf meltwater
85 concentrations (see Supporting Online Material, SOM) were 30-50% lower at these locations than during previous warm summers, and a weaker secondary meltwater maximum developed at around 600 m depth (Figs. 2B and S3). The reduced meltwater concentration is identifiable in temperature-salinity space (insert, Fig. 2A), where previous warm summer observations depart far less from a two-component mixture of CDW and meltwater. Geostrophic budgets of
90 dissolved oxygen, temperature and salinity at the ice front (26) show that meltwater production dropped from $\sim 80\text{ km}^3\text{ yr}^{-1}$ in 2009 (2) and 2010 (24) to $37\text{ km}^3\text{ yr}^{-1}$ in 2012 (Table 1), assuming that synoptic sections are representative of a short-term balanced state. This amounts to a 53% decrease in meltwater production, making the basal melting of PIB in summer 2012 the lowest on record, even below that estimated in 1994, when the warmest, deepest waters were $\sim 0.2^{\circ}\text{C}$
95 cooler at the glacier front.

To clarify links between ocean and basal melt variability, we use a state-of-the-art regional ocean-ice shelf model at 400-m resolution with the latest ice/seabed geometry (see SOM). When 2009 hydrographic conditions are imposed at its lateral boundaries (Fig. 3A), the model reproduces the main oceanographic features observed under the ice shelf by an autonomous

100 submarine (4). The ocean circulation and water properties are divided in two by the ridge (Figs. 3A and 3C). Offshore of the ridge, warm CDW circulates cyclonically after entering the cavity from the north, and then meanders back toward the ridge. Only the upper part of the CDW is able to flow over the ridge and reach the ice shelf grounding line. This CDW melts the ice, creating a colder, fresher, buoyant meltwater plume that rises along the ice shelf base (Fig. 3A). The vorticity created by this process and the cavity geometry impose a vigorous cyclonic circulation on the inshore side of the ridge, with near-seabed velocity reaching 0.2 m s^{-1} (Fig. 3C). The boundary between the inner and outer cavities is therefore marked by a dynamical front, further emphasizing (2, 4) the crucial role played by the ridge in controlling the ocean circulation and its interaction with the ice shelf. For 2009, the model simulates reasonable basal melt patterns (Fig. 110 1C) compared with observations (19, 20), producing $105 \text{ km}^3 \text{ yr}^{-1}$ of meltwater over the entire ice shelf (27, 28) and $86 \text{ km}^3 \text{ yr}^{-1}$ over its more commonly quoted fast-flowing southern part (2, 19, 24, see also SOM).

In sensitivity experiments, 1994 and 2012 hydrographic conditions were imposed at the lateral boundaries while keeping all other features the same (including ice geometry). For 2012, 115 the simulated cooling of the sub-ice cavity and diminished basal melting are consistent with the observed decrease in meltwater production. The lowered thermocline in 2012 reduces the amount of heat flowing over the ridge and cools the water that reaches the grounding line by 0.3°C (Fig. 3B). **In turn, melting is less pronounced and the buoyancy-driven circulation is concurrently decreased**, particularly in the inner cavity (Fig. 3D). Overall, the model estimates a 120 31-38% decrease in meltwater flux from the ice shelf in response to the cooling at its boundaries (Table S1). For 1994, when deepest waters are cooler than in 2012 but mid-depth waters are warmer, the model estimates only an 8-10% decrease in melting. These simulations neglect surface forcing and are limited by the imperfect seabed and constant ice geometry, which may explain the smaller reduction in melting than that observed. However, the model confirms the 125 large sensitivity of the present ice-ocean system to the depth of the thermocline relative to the ridge that is implied by the observations. The inability of the simulation to proportionally reproduce the 1994 melting level also suggests the importance of unresolved changes in cavity geometry between 1994 and 2009 (13).

If prolonged, the ocean conditions observed in January 2012 would have profound 130 implications for the PIG ice shelf. Continuation of a deep thermocline would reverse the current

ice-shelf thinning (as ice advection overcompensates the weakened basal melt), potentially permitting a re-advance of the grounding line. However, conditions in the months leading up to the 2012 observations were unusual (see also SOM). Most of 2011 was marked by strong easterly wind anomalies over the Amundsen Sea (Figs. 4A and 4B), weakening the typically cyclonic wind stress curl over the continental shelf (Fig. 4B) and curtailing the westerlies north of the shelf edge that are thought to enhance onshore CDW transport (21). Integrated over the preceding year, the zonal wind north of the continental shelf even reversed to easterly in 2011 (red line in Fig. 4B), an occurrence that is unique in the reanalysis wind record stretching back to 1979. Such conditions potentially decreased the flux of CDW onto the continental shelf and enhanced coastal downwelling, creating the 2012 thermohaline configuration with a relatively thin CDW layer in PIB.

The wind variability over the Amundsen Sea has both local and remote origins. In particular, convective anomalies in the equatorial Pacific troposphere are known to radiate an atmospheric wave train toward the area (29), affecting winds at the continental shelf edge. The strong easterly anomaly in January 2012 can be attributed to exceptionally weak convection in the western tropical Pacific associated with a significant La Niña event developing in late 2011 (Fig. 4C). The relevance of remote forcing from the tropical Pacific is illustrated by the statistically significant correlation (0.48) between the Niño 3.4 Sea Surface Temperature (SST) anomaly and the zonal wind over the continental shelf edge (Fig. 4A, see also SOM). While other factors affect the thermohaline structure in PIB, like eddy variability at the shelf edge (30), coastal downwelling (1) and buoyancy forcing (25, 26, 31), the conjunction of the January 2012 ocean conditions and the atmospheric anomalies in the preceding months confirms the important role of tropical forcing in determining the variability of melt rates under the PIG ice shelf (18).

Neighboring ice shelves closer to the continental shelf edge and exposed to greater ocean variability are naturally prone to a larger variability in melting (32). However, the presence of the ridge in front of the grounding line of PIG enhances its sensitivity to changes in oceanic/climatic forcing. Specifically, the blocking effect of the ridge makes the vertical distribution of heat a key element of the melting response. This study therefore stresses the importance of both local geometry and climate variability in determining ice shelf melting. With the added realization that this melting varies significantly over kilometer-scales (19, 20), and that oceanic variability is expected on intra-seasonal to interannual time scales, it is clear that

progress in the understanding and prediction of ice-sheet contributions to sea-level rise requires observations and models that capture a wide range of spatial and temporal scales.

165 **References and Notes:**

1. S. S. Jacobs *et al.*, The Amundsen Sea and the Antarctic Ice Sheet, *Oceanography* **25**, 154–163 (2012).
2. S. S. Jacobs, A. Jenkins, C. F. Giulivi, P. Dutrieux, Stronger ocean circulation and increased melting under Pine Island Glacier ice shelf, *Nat. Geosci.* **4**, 519–523 (2011).
- 170 3. S. S. Jacobs, H. H. Hellmer, A. Jenkins, Antarctic Ice Sheet melting in the southeast Pacific, *Geophys. Res. Lett.* **23**, 957 (1996).
4. A. Jenkins *et al.*, Observations beneath Pine Island Glacier in West Antarctica and implications for its retreat, *Nat. Geosci.* **3**, 468–472 (2010).
5. D. J. Wingham, D. W. Wallis, A. Shepherd, Spatial and temporal evolution of Pine Island
175 Glacier thinning, 1995–2006, *Geophys. Res. Lett.* **36**, L17501 (2009).
6. A. Shepherd *et al.*, A reconciled estimate of ice-sheet mass balance., *Science* **338**, 1183–9 (2012).
7. E. Rignot, Changes in West Antarctic ice stream dynamics observed with ALOS PALSAR data, *Geophys. Res. Lett.* **35**, L12505 (2008).
- 180 8. I. Joughin, E. Rignot, C. E. Rosanova, B. K. Lucchitta, J. Bolhander, Timing of Recent Accelerations of Pine Island Glacier, Antarctica, *Geophys. Res. Lett.* **30**, 1706 (2003).
9. I. Joughin, B. E. Smith, D. M. Holland, Sensitivity of 21st century sea level to ocean-induced thinning of Pine Island Glacier, Antarctica, *Geophys. Res. Lett.* **37**, 1–5 (2010).
10. H. D. Pritchard *et al.*, Antarctic ice-sheet loss driven by basal melting of ice shelves., *Nature*
185 **484**, 502–505 (2012).
11. A. Shepherd *et al.*, Recent loss of floating ice and the consequent sea level contribution, *Geophys. Res. Lett.* **37**, 1–5 (2010).
12. A. Shepherd, D. Wingham, E. Rignot, Warm ocean is eroding West Antarctic Ice Sheet, *Geophys. Res. Lett.* **31**, L23402 (2004).
- 190 13. J. W. Park *et al.*, Sustained retreat of the Pine Island Glacier, *Geophys. Res. Lett.* **40**, 2137–2142 (2013).
14. C. Schoof, Ice sheet grounding line dynamics: Steady states, stability, and hysteresis, *J. Geophys. Res.* **112**, 1–19 (2007).
15. S. S. R. Jamieson *et al.*, Ice-stream stability on a reverse bed slope, *Nat. Geosci.* **5**, 799–802
195 (2012).
16. G. H. Gudmundsson, J. Krug, G. Durand, L. Favier, O. Gagliardini, The stability of grounding lines on retrograde slopes, *Cryosph.* **6**, 1497–1505 (2012).
17. R. M. Gladstone *et al.*, Calibrated prediction of Pine Island Glacier retreat during the 21st

- and 22nd centuries with a coupled flowline model, *Earth Planet. Sci. Lett.* **333-334**, 191–199
200 (2012).
18. E. J. Steig, Q. Ding, D. S. Battisti, A. Jenkins, Tropical forcing of Circumpolar Deep Water
Inflow and outlet glacier thinning in the Amundsen Sea Embayment, West Antarctica, *Ann.
Glaciol.* **53**, 19–28 (2012).
19. P. Dutrieux *et al.*, Pine Island glacier ice shelf melt distributed at kilometre scales, *Cryosph.*
205 **7**, 1543–1555 (2013).
20. T. P. Stanton *et al.*, Channelized ice melting in the ocean boundary layer beneath Pine Island
Glacier, Antarctica., *Science* **341**, 1236–9 (2013).
21. M. Thoma, A. Jenkins, D. Holland, S. Jacobs, Modelling Circumpolar Deep Water intrusions
on the Amundsen Sea continental shelf, Antarctica, *Geophys. Res. Lett.* **35**, 1–6 (2008).
- 210 22. M. P. Schodlok, D. Menemenlis, E. Rignot, M. Studinger, Sensitivity of the ice-shelf/ocean
system to the sub-ice-shelf cavity shape measured by NASA IceBridge in Pine Island Glacier,
West Antarctica, *Ann. Glaciol.* **53**, 156–162 (2012).
23. P. Heimbach, M. Losch, Adjoint sensitivities of sub-ice-shelf melt rates to ocean circulation
under the Pine Island Ice Shelf, West Antarctica, *Ann. Glaciol.* **53**, 59–69 (2012).
- 215 24. Y. Nakayama, M. Schröder, H. H. Hellmer, From circumpolar deep water to the glacial
meltwater plume on the eastern Amundsen Shelf, *Deep Sea Res. Part I Oceanogr. Res. Pap.* **77**,
50–62 (2013).
25. A. A. Petty, D. L. Feltham, P. R. Holland, Impact of Atmospheric Forcing on Antarctic
Continental Shelf Water Masses, *J. Phys. Oceanogr.* **43**, 920–940 (2013).
- 220 26. P. R. Holland, A. Jenkins, D. M. Holland, Ice and ocean processes in the Bellingshausen Sea,
Antarctica, *J. Geophys. Res.* **115**, 1–16 (2010).
27. E. Rignot, S. Jacobs, J. Mouginot, B. Scheuchl, Ice Shelf Melting Around Antarctica,
Science (80-.). (2013), doi:10.1126/science.1235798.
28. M. A. Depoorter *et al.*, Calving fluxes and basal melt rates of Antarctic ice shelves., *Nature* ,
225 1–5 (2013).
29. Q. Ding, E. J. Steig, D. S. Battisti, M. Küttel, Winter warming in West Antarctica caused by
central tropical Pacific warming, *Nat. Geosci.* **4**, 398–403 (2011).
30. P. St-Laurent, J. M. Klinck, M. S. Dinniman, On the Role of Coastal Troughs in the
Circulation of Warm Circumpolar Deep Water on Antarctic Shelves, *J. Phys. Oceanogr.* **43**, 51–
230 64 (2013).
31. L. Padman *et al.*, Oceanic controls on the mass balance of Wilkins Ice Shelf, Antarctica, *J.
Geophys. Res.* **117**, 1–17 (2012).
32. S. S. Jacobs *et al.*, Getz ice shelf melting response to changes in ocean forcing, *J. Geophys.
Res. Ocean.* **118**, 1–17 (2013).
- 235 33. R. Timmermann *et al.*, A consistent data set of Antarctic ice sheet topography, cavity
geometry, and global bathymetry, *Earth Syst. Sci. Data* **2**, 261–273 (2010).

34. D. P. Dee *et al.*, The ERA-Interim reanalysis: configuration and performance of the data assimilation system, *Q. J. R. Meteorol. Soc.* **137**, 553–597 (2011).
- 240 35. A. Jenkins, The Impact of Melting Ice on Ocean Waters, *J. Phys. Oceanogr.* **29**, 2370–2381 (1999).
36. A. Jenkins, S. Jacobs, Circulation and melting beneath George VI Ice Shelf, Antarctica, *J. Geophys. Res.* **113**, 1–18 (2008).
37. M. Losch, Modeling ice shelf cavities in a z coordinate ocean general circulation model, *J. Geophys. Res.* **113**, C08043 (2008).
- 245 38. D. M. Holland, A. Jenkins, Modeling Thermodynamic Ice–Ocean Interactions at the Base of an Ice Shelf, *J. Phys. Oceanogr.* **29**, 1787–1800 (1999).
39. R. C. Pacanowski, S. G. H. Philander, Parameterization of Vertical Mixing in Numerical Models of Tropical Oceans, *J. Phys. Oceanogr.* **11**, 1443–1451 (1981).
- 250 40. J. Korona, E. Berthier, M. Bernard, F. Rémy, E. Thouvenot, SPIRIT. SPOT 5 stereoscopic survey of Polar Ice: Reference Images and Topographies during the fourth International Polar Year (2007–2009), *ISPRS J. Photogramm. Remote Sens.* **64**, 204–212 (2009).
41. P. Fretwell *et al.*, Bedmap2 : improved ice bed , surface and thickness datasets for Antarctica, *Cryosph.* **7**, 375–393 (2013).
- 255 42. A. Muto, S. Anandakrishnan, R. B. Alley, Subglacial bathymetry and sediment layer distribution beneath the Pine Island Glacier ice shelf, West Antarctica, modeled using aerogravity and autonomous underwater vehicle data, *Ann. Glaciol.* **54**, 27–32 (2013).
43. R. Robertson, Tidally induced increases in melting of Amundsen Sea Ice Shelves, *J. Geophys. Res. Ocean.* **118**, 1–8 (2013).
- 260 44. P. Gogineni, CReSIS Radar Depth Sounder Data, Lawrence, Kansas, USA. Digital Media. <http://data.cresis.ku.edu/>. (2012).
45. K. D. Mankoff, S. S. Jacobs, S. M. Tulaczyk, S. E. Stammerjohn, The role of Pine Island Glacier ice shelf basal channels in deep-water upwelling, polynyas and ocean circulation in Pine Island Bay, Antarctica, *Ann. Glaciol.* **53**, 123–128 (2012).
- 265 46. A. J. Payne *et al.*, Numerical modeling of ocean-ice interactions under Pine Island Bay’s ice shelf, *J. Geophys. Res.* **112**, 1–14 (2007).
47. A. Jenkins, K. W. Nicholls, H. F. J. Corr, Observation and Parameterization of Ablation at the Base of Ronne Ice Shelf, Antarctica, *J. Phys. Oceanogr.* **40**, 2298–2312 (2010).
48. E. Rignot, K. Steffen, Channelized bottom melting and stability of floating ice shelves, *Geophys. Res. Lett.* **35**, 2–6 (2008).
- 270 49. D. G. Vaughan *et al.*, Subglacial melt channels and fracture in the floating part of Pine Island Glacier, Antarctica, *J. Geophys. Res.* **117**, 1–10 (2012).
50. C. V. Gladish, D. M. Holland, P. R. Holland, S. F. Price, Ice-shelf basal channels in a coupled ice/ocean model, *J. Glaciol.* **58**, 1227–1244 (2012).
51. J. C. Comiso, Bootstrap Sea Ice Concentrations from Nimbus-7 SMMR and DMSP SSM/I-

- 275 SSMIS, [1978-2011], Boulder, Colorado USA: National Snow and Ice Data Center. Digital
media (2012).
52. A. K. Wåhlin, X. Yuan, G. Björk, C. Nohr, Inflow of Warm Circumpolar Deep Water in the
Central Amundsen Shelf*, *J. Phys. Oceanogr.* **40**, 1427–1434 (2010).
- 280 53. L. Arneborg, A. K. Wåhlin, G. Björk, B. Liljebladh, A. H. Orsi, Persistent inflow of warm
water onto the central Amundsen shelf, *Nat. Geosci.* **5**, 876–880 (2012).
54. D. P. Walker, A. Jenkins, K. M. Assmann, D. R. Shoosmith, M. A. Brandon, Oceanographic
observations at the shelf break of the Amundsen Sea, Antarctica, *J. Geophys. Res. Ocean.* **118**,
2906–2918 (2013).
- 285 55. R. L. Fogt, A. J. Wovrosh, R. A. Langen, I. Simmonds, The characteristic variability and
connection to the underlying synoptic activity of the Amundsen-Bellinghousen Seas Low, *J.*
Geophys. Res. Atmos. **117** (2012), doi:10.1029/2011JD017337.
56. Q. Ding, E. J. Steig, D. S. Battisti, J. M. Wallace, Influence of the Tropics on the Southern
Annular Mode, *J. Clim.* **25**, 6330–6348 (2012).
- 290 57. D. H. Bromwich *et al.*, Central West Antarctica among the most rapidly warming regions on
Earth, *Nat. Geosci.* **6**, 1–7 (2012).
58. J. P. Nicolas, D. H. Bromwich, Climate of West Antarctica and Influence of Marine Air
Intrusions, *J. Clim.* **24**, 49–67 (2011).
59. T. J. Bracegirdle, Climatology and recent increase of westerly winds over the Amundsen Sea
derived from six reanalyses, *Int. J. Climatol.* **33**, 843–851 (2013).
- 295 60. E. J. Steig *et al.*, Recent climate and ice-sheet changes in West Antarctica compared with the
past 2,000 years, *Nat. Geosci.* **6**, 372–375 (2013).

300 **Acknowledgments:** PD and JDR were supported by NERC grants NE/G001367/1,
NE/H02333X/1 and NE/J005770/1. HKH and SHL were supported by KOPRI grants
PP12010 and PP13020. The European Centre for Medium-Range Weather Forecasts is
acknowledged for serving the ERA-Interim reanalysis dataset, and CReSIS (with support
from NSF grant ANT-0424589 and NASA grant NNX10AT68G) is acknowledged for
generating and serving radar observations.

305

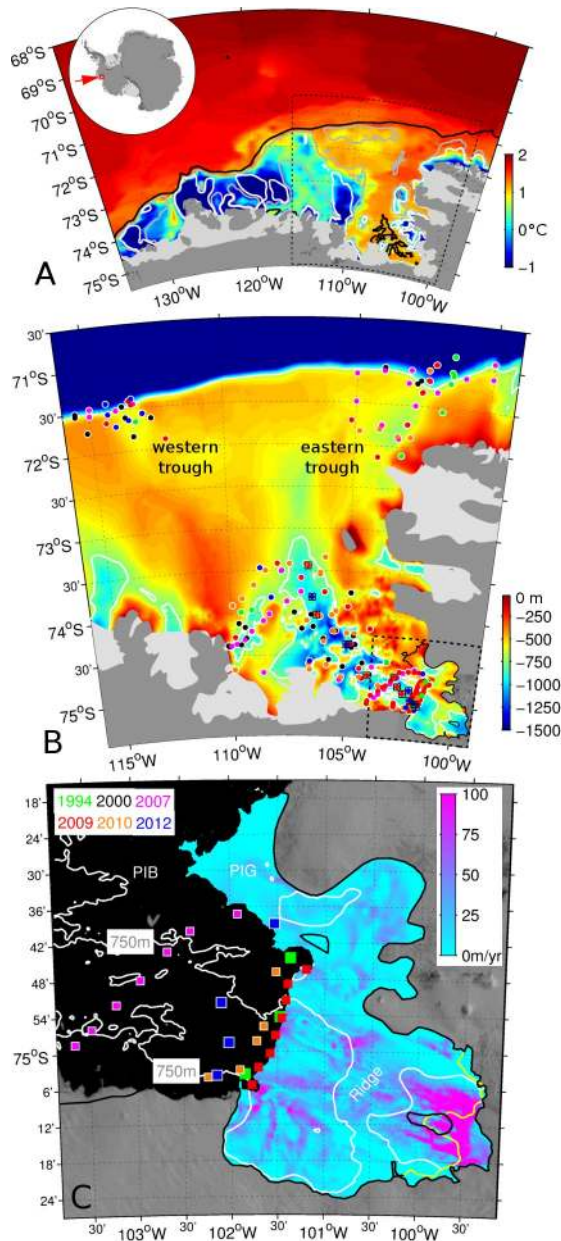
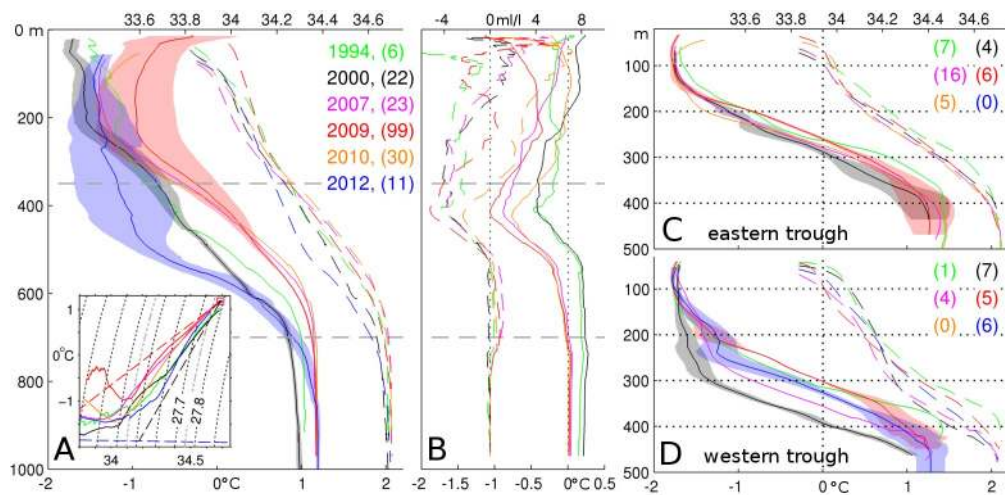


Fig. 1. Temperature maximum, seabed elevation and selected observation locations in the Amundsen Sea. **A.** Maximum sub-surface temperature deduced from a climatology of observations taken between 1994 and 2012 (SOM). Black, gray and white contours indicate seabed elevations (33) of -1000 m, -500 m and -400 m respectively. The dashed black box shows the area in B. **B.** Detailed bathymetry on the eastern Amundsen Sea continental shelf. The white line shows -750 m seabed elevation. Color-coded dots (squares) show ocean station positions used in Figs. 2, 3A and 3B. The dashed black box shows the area in C. The PIG ice shelf has been removed to show the seabed elevation beneath (SOM). **C.** 2009 coastline and ice shelf grounding line (9) are indicated by the black line. The yellow line shows the position of the grounding line in 1996 (7). Color-coded squares indicate ocean stations used to compute PIG ice shelf melt budgets. Simulated freshwater flux into the ocean (color) for 2009 boundary conditions.



320 **Fig. 2. Hydrographic properties in PIB.** **A.** Cruise-average, 25-dbar averaged temperature
 (continuous lines, shading indicates one standard deviation for selected years) and salinity
 (dashed lines) profiles from January-March 1994, 2000, 2007, 2009, 2010 and 2012 in the wider
 Pine Island bay (individual profile locations are shown in Fig. 1B, number of profiles per year
 are indicated in parentheses). Averages are performed in density-space and the resulting profiles
 325 regridded into pressure-space using the average stratification for each year. Dashed gray lines
 roughly indicate the 2009 ice front draft and the seabed ridge crest, respectively. Inset: the same
 data in potential temperature-salinity space, with the surface freezing line indicated in dashed
 blue, the 2009 CDW-glacial-ice melt line in dashed red, and the 2009 CDW-WW mixing line in
 dashed black. Black-dotted contours of potential density anomaly are also shown, with the
 330 isopycnals corresponding to the 2009 ice front draft and seabed ridge crest indicated in dotted
 gray. **B.** Mean 2012 offset from other years in potential temperature (continuous) and meltwater
 concentration (dashed) for all other observed summers (color-coded as in A). The difference is
 computed in density-space and then plotted in pressure-space using the mean 2009 stratification.
 335 **C.** Same as A, but for the near-shelf edge area to the east (see Fig. 1B). **D.** Same as A, but for the
 near-shelf edge area to the west (see Fig. 1B).

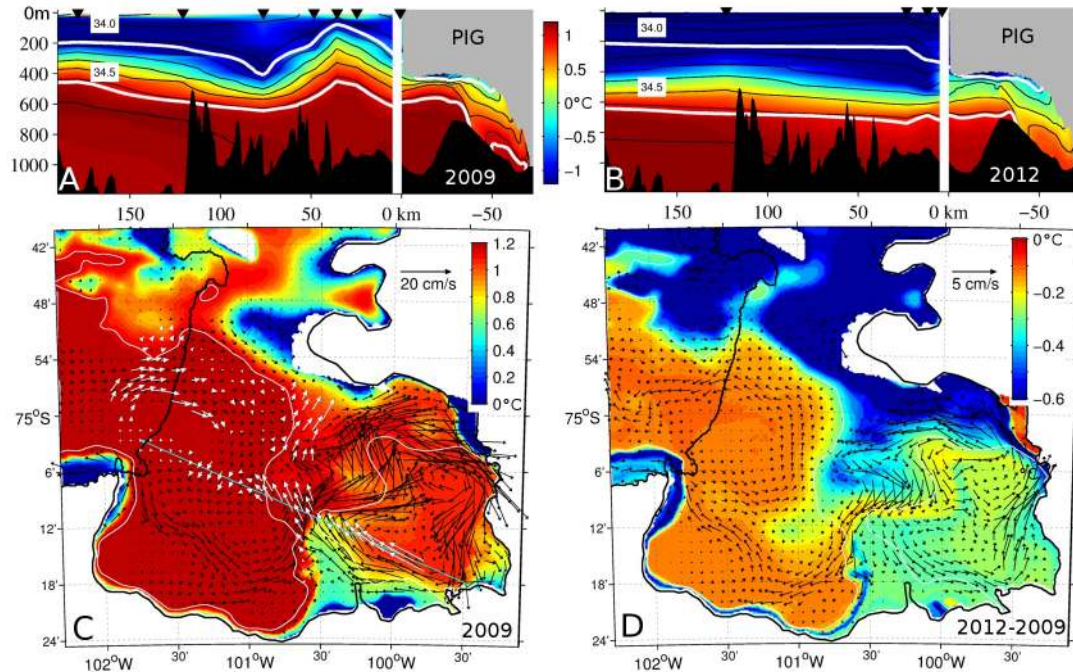


Fig. 3. Observed and simulated hydrography and circulation in 2009 and 2012. A. Section of observed and simulated 2009 potential temperatures (color) and salinity (black contours) along the eastern Amundsen Sea trough and underneath the PIG ice shelf. White lines show the surface-referenced 27.47 and 27.75 isopycnals. The panel shows observations outside the PIG cavity, and simulation results within it. Observations are linearly interpolated from profiles (black triangles) indicated in figure 1B. B. Same as A but for the 2012 observations and simulation. C. Modeled potential temperature (color) and velocity (black vectors, every fifth vector is shown) averaged within 50 m of the seabed for the 2009 simulation. White vectors show the corresponding velocity observed by Autosub (binned on the model grid, see also Fig. S2A). The cyan line indicates the position of the section used in panels A and B. The white line indicates 750 m seabed depth. D. Same as C but for the difference between the 2012 and the 2009 simulations.

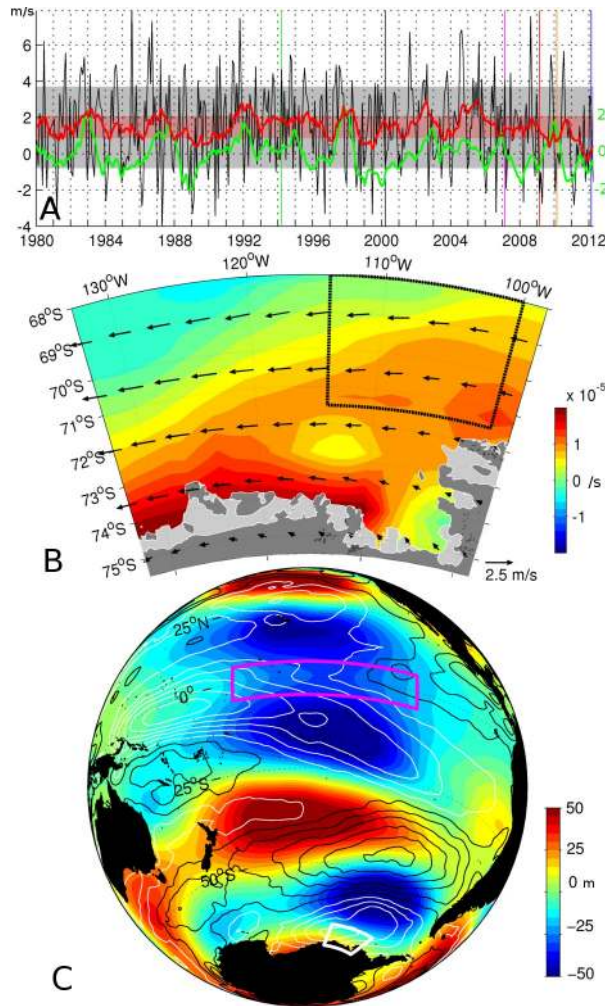


Fig. 4. Exceptional forcing prior to the 2012 anomaly. **A.** Monthly-mean 10-m-height zonal wind velocity (34, black) and its running integral over the preceding 12 months (red), averaging over the area indicated by the black-dotted box in **B**. Shaded areas indicate one standard deviation around the mean for each. The green line shows the SST monthly anomaly in the Niño 3.4 area. Dates of ocean observations are indicated by colored vertical lines. **B.** 2011 annual mean of anomalies in surface wind (vector) and wind-stress curl (color) with respect to the 1979-2011 monthly climatology of each. **C.** 2011 annual mean of anomalies in atmospheric geopotential height at 200 hPa (color) and sea surface zonal wind (contour) with respect to the 1979-2011 monthly climatology. White (black) contour are negative (positive), with 1 m s^{-1} interval. The white and magenta boxes indicate the area depicted in **B** and the Niño 3.4 area, respectively.

Year	Seawater transport			Meltwater transport		Max (Mean) correction cm s ⁻¹
	mSv		km ³ yr ⁻¹ (Iceq)	km ³ yr ⁻¹ (Iceq)		
	In	Diff	Diff	In	Diff	
1994	-245	1.45	51.3	-36.4	49.1	2.8 (2.1)
2007	-355	3.13	110.6	-61.3	107.3	2.6 (0.8)
2009	-401	2.26	79.7	-36.8	79.4	2.4 (1.4)
2010	-401	2.13	75.2	-43.4	69.2	2.8 (2.1)
2012	-357	1.06	37.3	-71	34.7	1.6 (1.3)

Table 1. Balanced-transport estimates. For each set of observations, transports are estimated by balancing geostrophic fluxes of temperature, salinity and dissolved oxygen budgets at the calving front of the ice shelf (see SOM), allowing for a barotropic adjustment of the geostrophic velocity profiles (last column). Seawater transport into the cavity (“In”) and net transport out of the cavity (“Diff”, positive outward) are given in mSv (1 mSv=10³m³ s⁻¹) and in equivalent of ice (Iceq) using a water density of 1030 kg m⁻³ and an ice density of 920 kg m⁻³. Employing the calculated meltwater fraction and balanced geostrophic velocity, meltwater transports are also shown. The fact that both transports do not depart significantly from each other is a consistency check. Note that 2007 observations were taken farther away from the ice front and thus are reflective of the entire ice shelf (27), while other years probably represent only the fast-flowing southern part of the ice shelf (see SOM). Transport estimates are typically subject to a methodological uncertainty of about 10% (2).

Supplementary Materials:

Materials and Methods

Figures S1-S10

380 Tables S1

References (35-59)

Supporting Online Material for:

385 **Strong sensitivity of Pine Island ice shelf melting to climatic variability**

Pierre Dutrieux, Jan De Rydt, Adrian Jenkins, Paul R. Holland, Ho Kyung Ha, Sang Hoon Lee, Eric J. Steig, Qinghua Ding, E. Povl Abrahamsen, Michael Schröder

390 In addition to a methods description, this supplementary note details the location of available historical observations and the geometry used in the ocean simulations, provides additional evaluation of the model against available observations, compares observation- and simulation-based meltwater budgets, and presents additional evidence of the influence of tropical forcing on zonal-wind variability in the Amundsen Sea area.

395

Methods:

For each austral summer, meltwater concentrations are calculated using temperature, salinity and dissolved oxygen observations and assuming all observations are produced by mixing three source water masses: CDW, WW and glacial meltwater (2, 35). In a similar manner to previous studies (2, 36), heat, salt and oxygen budgets can be balanced at the ice front to deduce the amount of melt occurring at the ice shelf base. Such estimates assume steady state ocean and sufficient sampling, and are typically subject to an additional methodological uncertainty of about 10% (2).

400 All model results presented in this study are obtained using the MITgcm z-level ocean model, which includes a static representation of ice shelves (37). The melt rate at the ice-ocean interface is computed from a three-equation formulation (38), with exchange coefficients depending on friction velocities at the ice-ocean boundary. Melting parameters are the same as in (38), except for the ice-ocean drag coefficient used to estimate turbulent exchange, which is tuned to the value of 5×10^{-3} to produce a melt-water volume close to that derived from observations in 2009 (see tables 1 and S2). The standard drag coefficient of 2.5×10^{-3} is used in the momentum equations. The model has horizontal and vertical resolution of 400 m and 20 m, respectively, and partial cells with a minimum thickness of 1 m allow the bathymetry and ice draft to be resolved at finer vertical scales. Advection is modeled by a 3rd order flux-limited advection scheme. The Pacanowski-Philander scheme (39) parameterizes vertical mixing. At the northern and western lateral boundaries, where no ice shelf is present, temperature and salinity are restored to ice-front-averaged observed conditions, and free-slip boundary conditions are applied on all vertical walls, including at the northern and western lateral boundaries. Zero-flux conditions are used at the open-ocean surface. All results are averaged over the 8th month of simulation, when a quasi-steady-state is reached, but the circulation within the cavity and the associated melt rates reach 95% of their final magnitude within 2 months.

420

Historical observations in the Amundsen Sea:

425 To our knowledge, a total of 1223 CTD profiles have been taken to date in and near the Amundsen Sea since 1994 (Fig. S1). This collection spans nearly two decades, with a clear sampling bias towards recent years. A detailed analysis of this dataset is beyond the scope of this study, but a climatological grid was built from all available observations and used for illustrative purposes in Fig. 1a. Only regional subsets of those observations used in Fig. 2 are displayed in Fig. 1B.

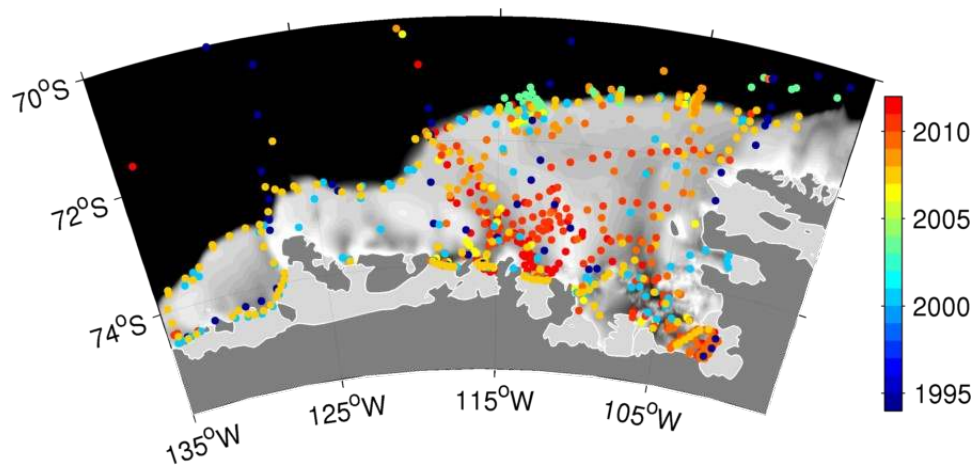


Fig. S1. CTD profile database. The positions of profile observations made in the Amundsen Sea are indicated by dots color-coded by their observational time.

430

High-resolution ice and seabed geometries:

Modeling the ocean circulation and ice-ocean interaction beneath the PIG ice shelf requires a detailed knowledge of the ice and seabed geometry. The available Autosub (4) track lines provide highly accurate but sparse samples of both. Complementary larger-scale, less accurate datasets are therefore used to fill gaps. All data are linearly interpolated on a 100 m-resolution grid.

A 40 m-resolution digital elevation model (DEM) of ice freeboard from the SPIRIT project (19, 40) is used to calculate ice draft by assuming freely-floating ice with a density of 918 kg m^{-3} and 12 m of air within the firn. The DEM dates from March 2008, and is adjusted using a constant median bias from the 2009 Autosub ice draft observations. On the slower-flowing portions of the ice shelf, 2009 radar lines from the IceBridge project provide additional information (Fig. S2A). In poorly sampled areas and close to the grounding line where the assumptions underpinning the estimates of depth from free-board may not hold, the gridded ice draft is less accurate.

The seabed elevation over the continental shelf is well known from ship echo-sounding (41). Under the ice shelf, a 2.5-km resolution, $\pm 150 \text{ m}$ -accuracy grid (M. Studinger, personal communication, and Fig. S2C) obtained from inversion of gravimetry data is corrected at each point using the median difference from all Autosub observations within a 6 km radius (Fig. S2C). The bias between the inverted gravimetry and Autosub observations indicates a strong east/west asymmetry from the ridge crest, perhaps suggesting that a sediment layer on the outer slope of the ridge, deposited when the ice was grounded on the ridge crest (4), is unaccounted for in the gravimetry inversion (42). In any case, our deduced bathymetry differs significantly from that directly obtained by gravimetry inversion and used in previous model experiments (22) since it does not contain a channel allowing access of warm deep waters to the ice shelf grounding line, but presents the continuous blocking ridge suggested by Autosub observations.

The final bathymetry (Fig. S2D) and ice draft (Fig. S2B) thus obtained are smoothed using a 5-point square-box smoothing to produce the final model grids.

460 **Evaluation of the simulations:**

The purpose of the numerical simulations is to represent the response of the ocean and induced ice shelf melt to variability in the wider Amundsen Sea. Doing so requires a state-of-the-art ocean model with an adequate representation of ice shelf/ocean interactions at sub-kilometer grid resolution (19). Simulating a large domain at such resolution is not practical. We thus opted
465 for a small domain covering the cavity beneath the ice shelf and part of Pine Island Bay, and make the assumption that adjustment of the cavity circulation to oceanic variability in the wider Amundsen Sea is fast compared to the time scale of that variability. Since the model adjustment is of order of months (95% of the quasi-steady state melt estimate is reached within 2 months), this assumption is probably valid for seasonal to interannual variability. Recent work suggest that
470 tidal variability leads to only weak variations in melt (43). However, time-scales shorter than seasonal are arguably more problematic and will need to be investigated in the future.

Although the geometry presented above is constrained as much as possible, some uncertainties remain, especially in areas unsampled by Autosub. These presumably have an important impact on the details of the ocean circulation. Similarly, missing components of the
475 forcing (tides, open-ocean surface wind and buoyancy fluxes) might play a role. The extent to which these factors affect the model results can be examined by comparing the simulation using mean observed 2009 hydrographic conditions at its lateral boundaries with the 2009 observations of sub-ice shelf currents and hydrographic properties made by Autosub (4).

Only the downward-looking Acoustic Doppler Current Profiler (ADCP) mounted on
480 Autosub was functioning with sufficient precision to determine ocean currents. The synoptic, near-seabed (average 20-50 m above the bottom) velocity is presented here (Figs. S3A-C, see also Fig. 3A), and can be compared with the monthly averaged current in the simulation. Given our assumptions and caveats, the level of agreement is good: the simulation reproduces the cyclonic gyres in the inner and outer cavities, and the asymmetry in velocity magnitude on either
485 side of the ridge. A weaker, more southerly located inflow over the ridge crest is present in the observation, but the Autosub sampling is limited along the top of the ridge and in the southwestern portion of the cavity, preventing a detailed evaluation of the sinuous simulated flow in other areas. For example, a deep current from the southern end of the ice front feeds the ridge overflow in the model: this feature is partly induced locally by a poorly-sampled deepening in
490 the bathymetry.

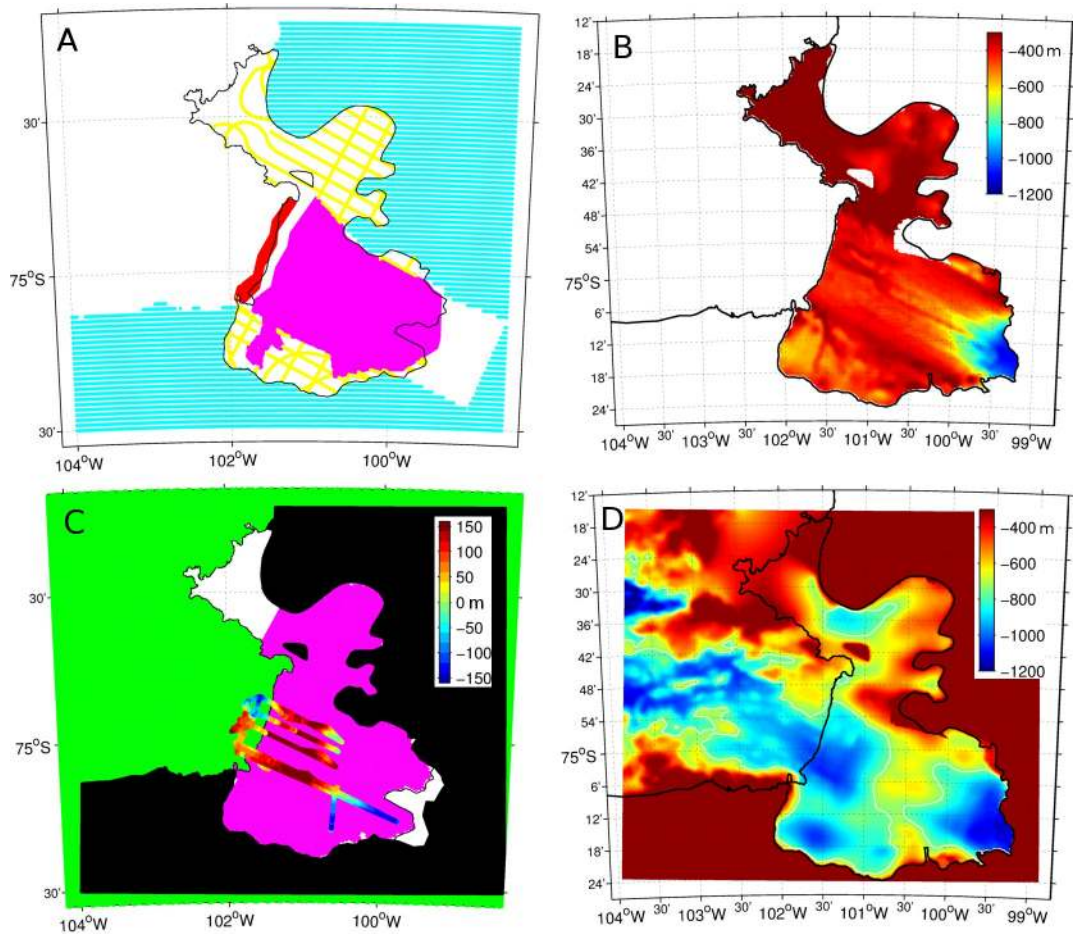


Fig. S2. Observations used to define the cavity geometry beneath the ice shelf. **A.** The grounded ice base is defined by previous airborne radar observations (33) gridded at the cyan dots. Over most of the fast-flowing part of the ice shelf, a 40-m resolution digital elevation model (19, 40) of the ice surface in March 2008 is inverted for ice draft (magenta), and the near-calving front geometry of 2008 is repeated (red) to account for the glacier advance in 2009. Over the remaining part of the ice shelf, 2009 airborne radar observations (43, yellow dots) measured the ice draft. **B.** Ice draft interpolated on the 400-m resolution model grid. The black contour defines the coastline and ice shelf edge in 2009. **C.** The seabed elevation beneath grounded ice is defined by previous airborne radar observations (33, black dots). The seabed elevation beneath the ice shelf is deduced by gravimetry (magenta dots, M. Studinger, personal communication) corrected to fit available Autosub observations within a 6 km radius. The difference between Autosub seabed elevation observations and the elevation inverted from the gravimetry data is shown by colored dots. Seabed elevation in open ocean and unmodeled areas (green dots) is known from ship echosounding (41). **D.** Seabed elevation interpolated onto the 400 m resolution model grid. The white contour delineates the 750 m isobath.

495 Consistent with the circulation, the model reproduces the hydrographic front over the seabed ridge. This front is visible in temperature (Figs. S3D-F), salinity (not shown) and oxygen (in observation only, not shown), as the ice melt-induced cold, fresh and oxygenated buoyant plume rises up the ice base and over the warm, saline and old (deoxygenated) Circumpolar Deep Water (CDW).

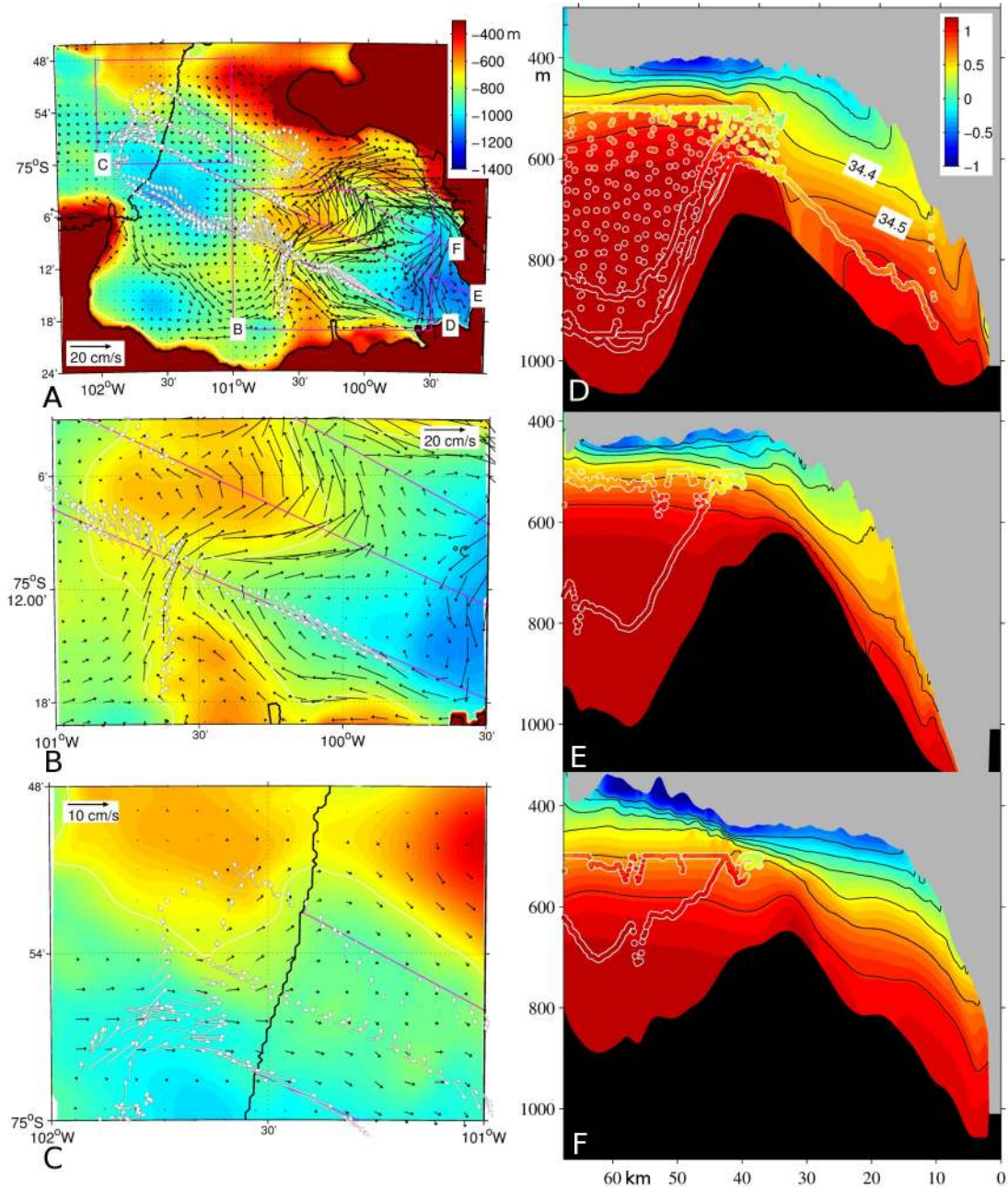


Fig. S3. Model evaluation. A. Simulated (black vectors, every fifth vector is shown) and observed (white vectors, 1 in 400 is shown) velocity 50 m from the seabed (colors) using the simulation forced with 2009 hydrographic conditions. The 2009 ice shelf boundary is delimited by the black line. The white contour delineates the 750 m isobath. Magenta lines show the position of sections in panels D-F. B-C. Enlargement of A in selected areas (magenta squares indicated in A). D-F. 2009 simulated potential temperature (color) and salinity (black contours) sections, directly compared with 2009 observations of potential temperature (white-circled color dots, 1 in 50 is shown) made by Autosub within 2 km of the sections.

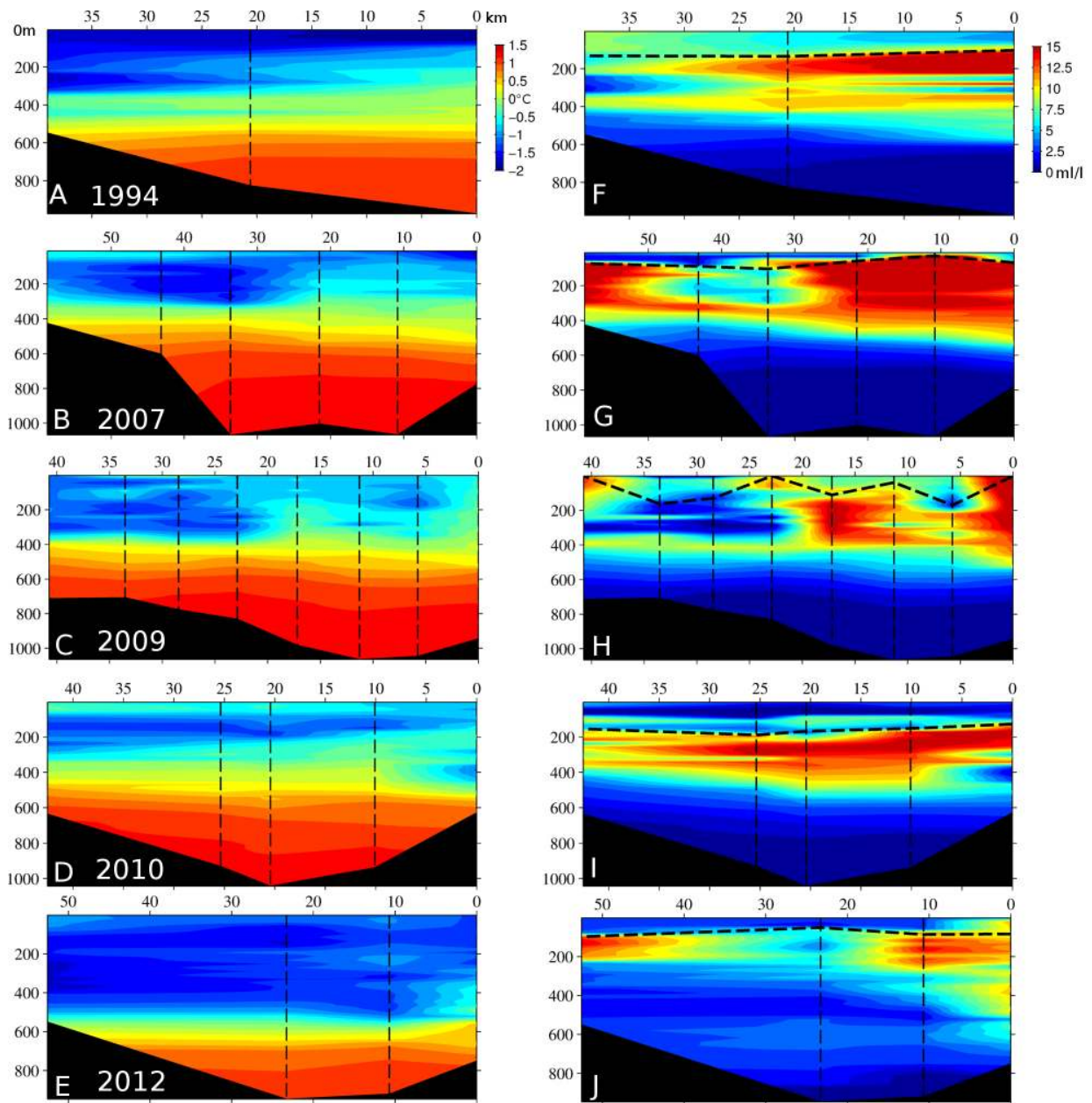
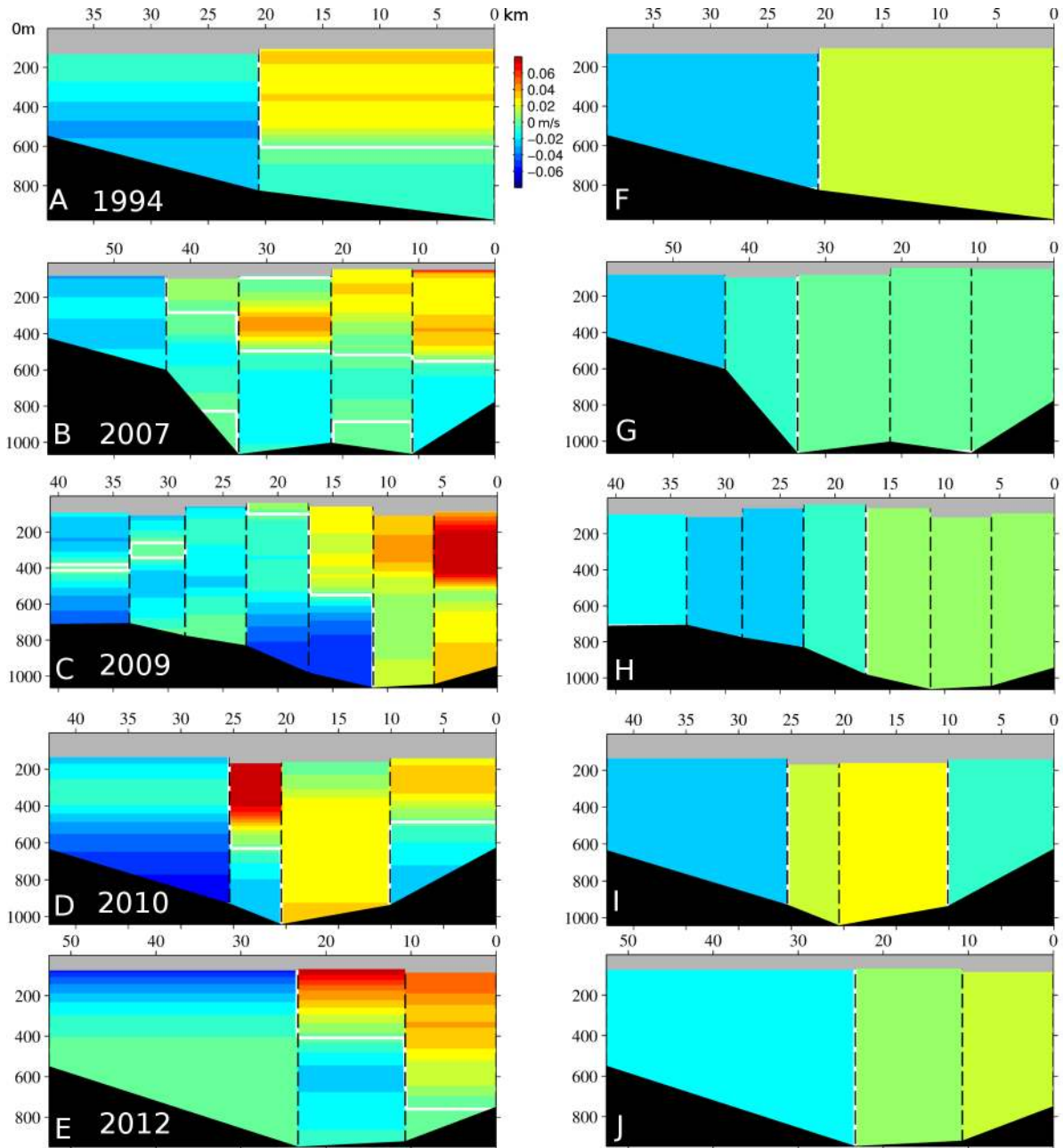


Fig. S4. Calving front observations. Potential temperature (A-E) and meltwater fraction (F-J) sections at the PIG ice shelf calving front for individual years of observation (labeled). Sections are drawn from north (left) to south (right), thus facing into the cavity beneath the ice shelf. Note that both axes vary in scale between years. In addition to those situated at either end of the sections, hydrographic profile positions are indicated by black vertical dashed lines. Contours are linearly interpolated on a grid with 25-m resolution in depth and 1-km in distance. In F-J, the thick dashed black line indicates the threshold depth above which meltwater fraction calculations are assumed to be unreliable because of the impact of air-sea exchanges on water properties.



520 **Fig. S5. Calving front balanced velocity.** Sections of adjusted geostrophic velocity (A-E) and
 associated barotropic adjustment (F-J) to the original geostrophic velocity across the PIG ice front for
 individual years of observation (labeled). Sections are drawn from north (left) to south (right), thus
 facing into the cavity beneath the ice shelf. Note that both axes vary in scale between years. In addition
 525 to those situated at either end of the sections, hydrographic profile positions are indicated by black
 vertical dashed lines. Contours are linearly interpolated on a grid with 25-m resolution in depth and 1-
 km in distance. White contours indicate zero velocity. Positive velocities are out of the cavity.

However, the model does not capture the exact location of the front. For example, the model does not show the right strength or location for the jet along the ridge line, and the

530 thermocline in figure S3D (S3F) is too high (low) compared with Autosub observations. These
discrepancies could be due to either inaccurate geometry of the cavity where Autosub
observations are absent, high-frequency variations in the front location and strength, or even poor
parameterization of horizontal and vertical mixing. In general, however, the model reproduces
key characteristics of the frontal structure under the ice shelf, and it is therefore suitable for our
sensitivity experiment.

535

Observation-based meltwater budgets:

Hydrographic conditions near the ice front were sampled in austral summer 1994, 2007,
2009, 2010 and 2012 (Fig. S3). Although the location of the sections differs from year to year,
dictated by the sea-ice conditions and the ice front advance and calving cycle, all the presented
540 sections were made within a kilometer of the first direct contact between waters exiting the
cavity underneath the ice shelf and the atmosphere. It is therefore expected that in all of these
sections, the main driver of the circulation and water mass modification is the ocean-ice shelf
interaction. Assuming, for each sampled year, that all waters are a mixture of three sources (35),
t temperature, salinity and oxygen are used to compute the concentration of meltwater. Potential
545 temperature and meltwater concentration sections (Fig. S4) provide a general view of the oceanic
variability at the PIG ice front and the particularly anomalous character of 2012.

Interleaving the typical Winter Water (WW) above CDW stratification, warmer than
ambient meltwater outflows can be seen at the base of the thermocline and up to the near-
surface. Major channeled outflow locations (better sampled in 2009) can sometimes be identified
550 (45), but a clear Coriolis-driven tendency for CDW to enter the cavity at depth and from the
north and for meltwater within the outflows to be enhanced in the southernmost part is evident in
all sections (46). The adjusted geostrophic velocities across the sections (Fig. S5) provide
concrete support for this general feature of the circulation. The section made in 2012 shows a
diminished amount of heat available at the calving front with a deeper thermocline, and reduced
555 meltwater concentrations.

Using a method described previously (36), heat, salt and oxygen budgets can be balanced
to deduce the amount of basal melt occurring at the ice shelf base. Such estimates assume steady
state and sufficient sampling (see also 2 or an analysis of potential sampling bias in 1994), and
are typically subject to an additional methodological uncertainty of about 10%. However they
560 provide circulation patterns, basal ice shelf melt budget quantification and variability that are
consistent with physical principles, and we expect such estimates to be generally realistic. They
are shown for all sampled years in Table 1.

All years marked by an elevated thermocline and increased CDW core temperature,
namely 2007, 2009 and 2010, show similar net fluxes of meltwater coming from underneath the
565 ice shelf. 2009 and 2010 saw transports of 79.7 and 75.2 km³ yr⁻¹ ice equivalent (iceq) emanating
from beneath the fast-flowing part of the ice shelf, respectively. In 2007, part of the bay area was
covered by land-fast sea ice, so the observations were taken further north (Fig. 1C) and the
budget is probably more representative of the entire ice shelf, including its slow-flowing northern
part. This results in a larger transport estimate of 110.6 km³ yr⁻¹ (iceq) for similar hydrographic
570 conditions in PIB, equivalent to melting ~101.8 Gt yr⁻¹ of ice, in close agreement with the
101.2±8 Gt yr⁻¹ estimated from glaciological observations between 2003 and 2008 (27).
Equivalent proportions of basal melt under the southern and northern/slow-flowing parts of the
ice shelf are reproduced in the simulation (see year 2009 in Table S1). The consistency of the
results found for years with similar hydrographic conditions in PIB and small expected changes

575 in the shelf geometry between 2007 and 2010 further validates the budget methodology.

Other years with less available heat at the calving front saw reduced basal melt resulting in lower seawater transport from the cavity. In 1994, a transport of $51.3 \text{ km}^3 \text{ yr}^{-1}$ (iceq) is estimated in Table 1 (see also ref. 2), and 2012 stands out as a 53% decrease from 2009 with $37.3 \text{ km}^3 \text{ yr}^{-1}$ (iceq) transport.

580

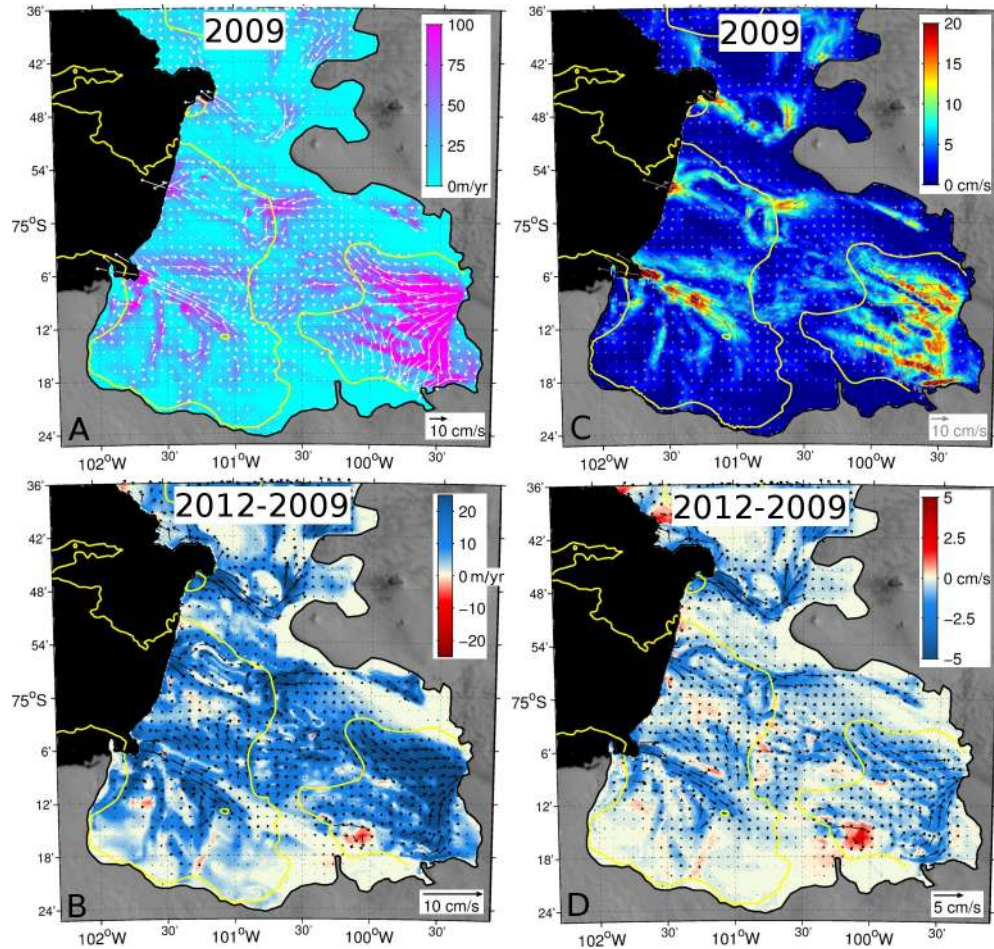


Fig. S6. Simulated melting. **A.** Simulated freshwater flux into the ocean (color) and ocean currents within 50 m of the ice shelf (white vectors) for a simulation using 2009 boundary conditions. The 750 m bathymetric contour is shown in yellow. The 2009 edge of the ice shelf is shown in black. **B.** Same as A, but showing the difference in melting and sub-ice shelf flow between the 2012 and 2009 simulations. Positive freshwater flux anomaly implies more rapid melting in 2012 than in 2009. **C.** Same as A, but with color showing simulated ocean currents within 50 m of the ice shelf. **D.** Same as B, but with color showing difference in simulated ocean currents within 50 m of the ice shelf between the 2012 and 2009 simulations.

Simulation-based meltwater budgets:

585 The drag coefficient within the three-equation melting parameterization (see Methods) is tuned in the 2009 simulation to roughly reproduce the total meltwater flux estimate from the 2009 observations. Though generally treated as an unvarying physical quantity, beneath PIG this drag coefficient is used to allow the model to represent the high spatial variability of the ice shelf base (19), which is still sub-grid-scale even in these high-resolution simulations. The final value

used (5×10^{-3}) is close to that used on Ronne ice shelf (47). Keeping the cavity geometry constant, a suite of sensitivity experiments are performed by changing the hydrographic conditions to which the model is restored along its open-ocean boundaries. Here we report the results of simulations in which hydrographic conditions appropriate to 1994, 2009 and 2012 were imposed.

The simulated reduction in basal melt in 2012 with respect to 2009 is less than that deduced from observations (compare Tables 1 and S1), but still reaches 31% over the fast-flowing part of the ice shelf. For 1994 the simulated basal melt is intermediate between 2009 and 2012, in agreement with the observation that the 1994 thermocline depth is intermediate between 2009 and 2012. However, the proportional change is lower than that observed: modeled 1994 equivalent ice fluxes represent 92% of those in 2009, compared with 64% in the observations. This discrepancy could be explained by inaccurate forcing and parameterizations in the model, but we suspect that neglected changes in the cavity geometry from 1994 to 2009 play a greater role. A change in the area subject to melting is expected to have a relatively large impact on melt, and the grounding line movements from 1996 to 2009 (Fig. 1C) imply an enlargement of the ocean cavity that is unaccounted for in the model. Grounding line migration between 2009 and 2012 is arguably less important during the shorter (3 years) time span (13).

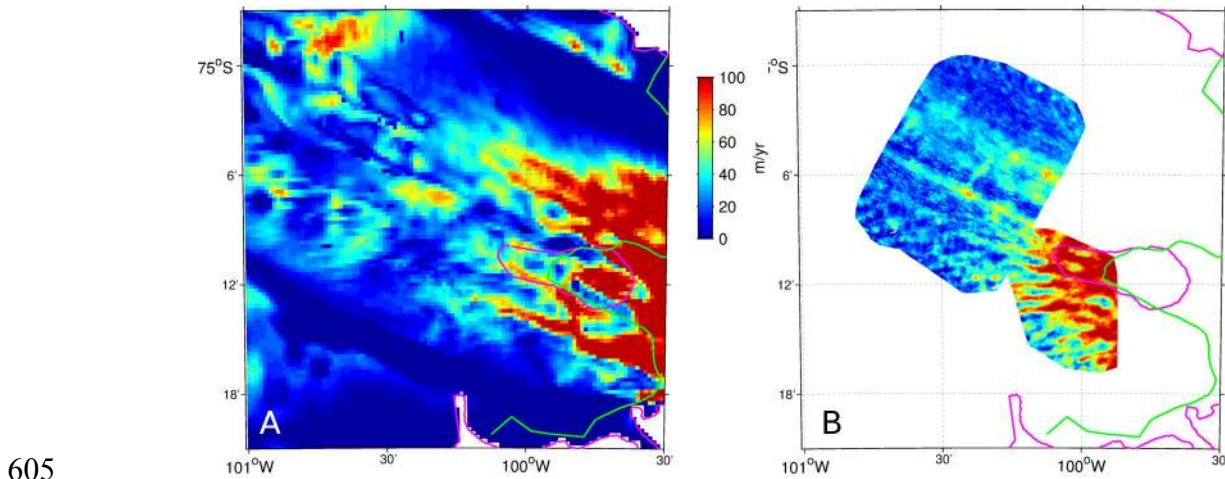


Fig. S7. Melting in model and observations. A. Simulated freshwater flux into the ocean (color) for a simulation using 2009 boundary conditions. The 2009 (1996) grounding line of the ice shelf is shown in magenta (green). B. Same as A, but from observations using a Lagrangian comparison between surface elevation products (19).

Maps of basal melting and the near-ice ocean circulation are shown in figure S6 and are compared with observation-based estimates in figure S7. On the large scale (>5 km), melt is concentrated near the grounding line and is simulated to reach 120 m yr^{-1} in 2009 (figures S6a and S7), in agreement with observations (19). Outflows at the ice front are directed by the broad-scale topography of the ice-shelf base, and are concentrated in three main parts, near the south, the center and the north of the ice shelf fast flowing part. This is consistent with observations (45, see also Figs. S4 and S5) and earlier simulations using a smoother geometry and simpler 'plume' ocean physics (46). At the smaller scale (<5 km), ocean flows and melting tend to be structured by resolved basal channels, near the grounding line and in the southern portion of the ice shelf, and ocean currents within channels typically reach 10 cm s^{-1} , close to observations (20).

620 We note here however that even at 400-m resolution, kilometer-scale channels remain poorly represented (Fig. S7). The correlation between basal melt and basal channels under ice shelves has important implications for the dynamics of the ice-ocean interaction (19, 48–50), and we assume here that the model representation of these features is sufficient for our sensitivity study. Changing hydrographic conditions modulates the amplitude of melting and associated circulation (Figs. S6B and S6D), but not its general spatial distribution.

Year	Simulated freshwater flux			
	Entire ice shelf		Fast flowing part only	
	total (km ³ yr ⁻¹)	% of 2009	total (km ³ yr ⁻¹)	% of 2009
1994	91.6	87	79.5	92
2009	105.4	100	86.4	100
2012	65.6	62	59.4	69

625 **Table S1. Net simulated freshwater fluxes under the ice shelf.**

Sea ice conditions in the months leading up to January 2012:

630 In summer 2010, the sea-ice concentration in the eastern Amundsen Sea was the lowest on record (Fig. S8A). Though sea-ice advection through this region is important, this probably implies that local sea-ice production in the following autumn was larger than usual, potentially creating a thick layer of WW in PIB. However, the austral summer preceding that of 2012 actually saw relatively high sea-ice concentrations and it is unclear whether the potential anomaly in WW thickness of 2010 would have persisted throughout the following year leading up to January 2012. Given the importance of sea-ice processes for modifying hydrographic properties in polar regions, we suspect they are also playing a role in setting the 2012 anomaly, but cannot quantify such effect with confidence. If ice growth in 2010 did create a long-lasting anomaly, the impact on the ice shelf should be visible in altimeter records.

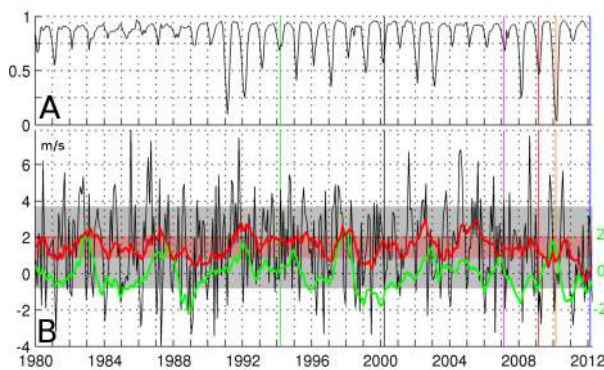


Fig. S8. Sea-ice and zonal wind variability. A. Average sea ice concentration (5I) in the eastern Amundsen Sea. Dates of ocean observations are indicated by colored vertical lines (color code defined in Fig. 1). B. Same as Fig. 4A. Monthly-mean 10-m-height zonal wind velocity (black) and its running integral over the preceding 12-month (red), averaging over the area indicated by the black-dotted box in Fig. 4C. Shaded areas indicate one standard deviation around the mean for each. The green line shows the SST monthly anomaly in the Niño 3.4 area.

640

Characterization of the atmospheric bridge between the ASE and the tropical Pacific:

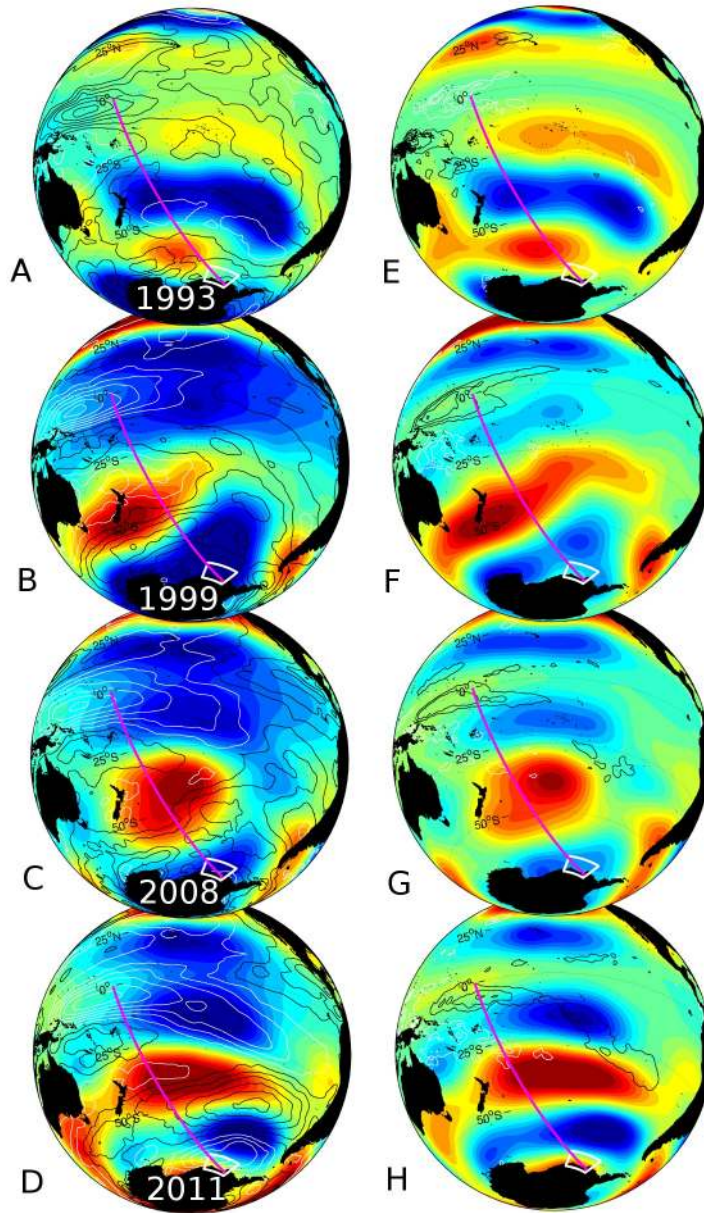
645 Relatively coarse regional ocean simulations identified a link between zonal wind
variability over the continental shelf edge of the Amundsen Sea and the on-shelf inflow of warm
CDW (21). In this model, wind anomalies generated fluctuations in the flux of warm water in the
ASE, and PIB, dominating over the local wind and buoyancy forcing of upper water column
properties. In turn, variations in the volume of heat in PIB were expected to impact ice shelf
650 melting, although the latter was poorly represented by limited resolution and the unknown under-
ice-shelf bathymetry at the time. In this model, the time-scale necessary for a shelf-break
anomaly to reach PIB is of the order of a few months. However, we can expect that other,
unresolved shelf-break processes involved in feeding CDW to PIB also play a role in modulating
hydrographic properties in PIB while the focus on seabed rather than mid-water column
655 processes will have downplayed the role of surface forcing within PIB. Since such processes
likely operate over a wide range of time-scales, the ocean state observed at any given time is
expected to reflect the non-linear sum of all processes.

Analysis of atmospheric reanalysis products has demonstrated a statistically significant
relationship between the tropical Pacific and the zonal wind in the Amundsen Sea area (18). In
660 general, increased westerly wind stress over the continental shelf edge is associated with El Niño
conditions; easterly anomalies are associated with La Niña conditions. Figures 4A and 4C in the
main text illustrate these points: (1) correlation between zonal wind over the ASE and sea
surface temperature (SST) in the Niño 3.4 region is 0.48, suggesting that about 25% of the
interannual variability of the zonal wind in the ASE can be attributed to variability in the tropics;
665 (2) the mechanistic link between the two regions is a standing atmospheric wave radiating from
the central equatorial Pacific (29).

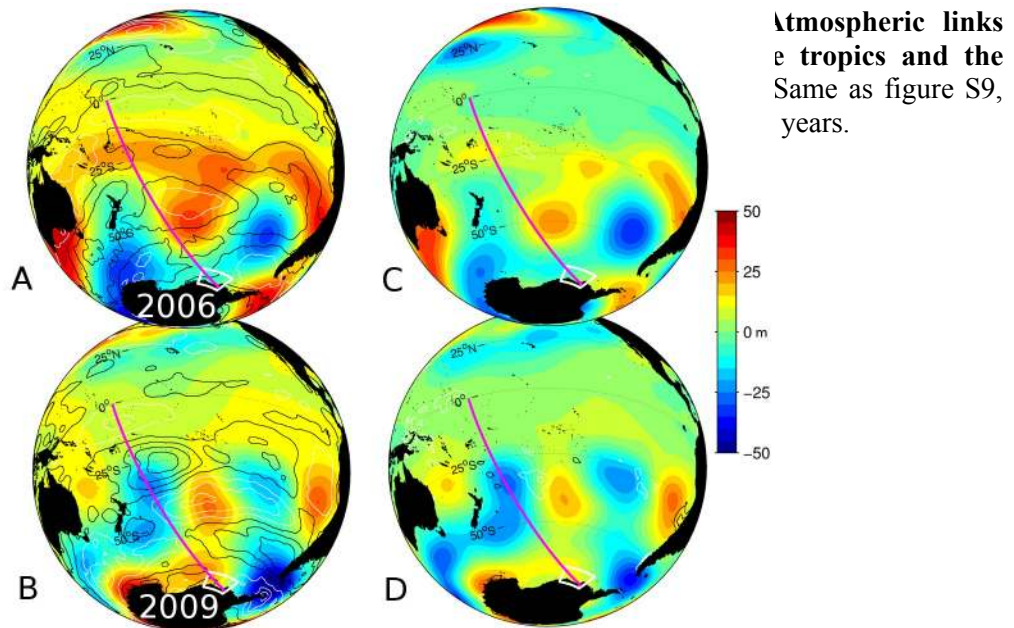
Figure S9 illustrates the anomalous conditions of 2011 compared with other selected
years relevant to ocean observations in PIB. In the annual average for 1993, there are positive
anomalies in 200 hPa heights in the tropics (Figs. S9A and S9E) and north of the Amundsen Sea,
670 showing a classic Rossby-wave pattern. These are accompanied by anomalous deep convection
(negative Lagrangian rate of change of pressure with time, ω) in the tropical Pacific, shown by
the white contours in figure S9E. In contrast, 200 hPa height anomalies in 1999, 2008, and 2011
are negative over the tropics and high latitudes, and convective anomalies are negative (positive
 ω). In 2011 only, the wind stress anomalies over the Amundsen Sea Embayment are strongly
675 negative (easterly); this is accompanied by more widespread and convective anomalies, centered
near the dateline in the tropical Pacific.

Given the large scale of the atmospheric circulation anomalies compared to the small size
of the ASE, one can expect that spatial variations in the Rossby-wave source or variations in the
source amplitude will have major impacts on the resulting wind anomaly in the ASE. For
680 example, although 1999 was a La Niña year like 2011, and the deep-convection anomaly was of
the same intensity as that of 2011, it was centered west of the dateline, leading to a southward
wave radiation that impacted the Ross Sea sector more than the Amundsen Sea sector. The result
was a weak zonal wind anomaly over the ASE. In 2008, the deep-convection anomaly was
weaker than either during 1999 and 2011, and also centered to west of the dateline. The resulting
685 wave train was then neither properly centered nor had sufficient amplitude to have a large impact
on the zonal wind over the ASE.

In 2006 and 2009 (Fig. S10), there are no clear deep-convection anomalies in the tropics, and no
evidence of Rossby wave propagation is apparent in the anomaly field.



Atmospheric links between the ASE and the ASE.
 The ERA-Interim annual average of the 10-metre wind anomaly on the left (A-D) and of 10-metre wind anomalies with a frequency of 50° per year on the right (E-H). Note that the color scale is the same for both columns. The white diamond is the pole, and the pink line is the 50 hPa level. The color scale for the left column shows annual wind anomalies (m s⁻¹) and for the right column shows high-pass-filtered wind anomalies with a frequency of 50° per year (m s⁻¹). The color scale for the left column ranges from -50 to 50 m s⁻¹ (white is zero), and for the right column from -0.02 to 0.02 Pa s⁻¹ (white is zero).



These simple diagnostics reveal that although a clear connection exists between deep-
 convection anomalies in the equatorial Pacific and zonal wind over the ASE, the convective
 anomalies need to be at the relevant longitude and of sufficient amplitude to have a large impact.
 Furthermore, the link between the zonal wind anomaly and ocean properties in PIB is not a
 695 direct, linear one, as energy from the wind is passed down to the ocean, and ocean processes at
 the continental shelf edge adjust to the surface forcing. Therefore, we expect that only major
 anomalies in the wind, such as occurred in 2011, will be followed by identifiable anomalies in
 the flux of CDW onto the intermediate to lower oceanic layers in the ASE, and hence in the
 700 thermohaline structure in PIB.

More work is required to better understand the oceanic variability in PIB, its causes and
 likely impacts. Specifically, at the regional level, an improved understanding of the processes
 driving the flux of CDW in the ASE at the shelf edge (30, 52–54) and of the processes
 controlling the thermohaline structure in PIB is needed. On a more global scale, a detailed
 705 review of factors influencing the wind over the ASE, including but not limited to the tropical
 Pacific, including synoptic (55), interannual (18, 56–59), decadal and longer (60) timescales,
 would be beneficial.